Modeling fully nonlinear wave-structure interaction by an adaptive harmonic polynomial cell method with immersed boundaries

Chao Tong[1*], Yanlin Shao[1,2], Harry B. Bingham[1]

1: Department of Mechanical Engineering, Technical University of Denmark, 2800 Lyngby, Denmark
2: College of Shipbuilding Engineering, Harbin Engineering University, 150001 Harbin, China

1 Introduction

We proposed a 2D high-order immersed-boundary adaptive harmonic polynomial cell (IB-AHPC) method for solving fully-nonlinear wave-structure interaction problems based on potential-flow theory. Unlike the methods using overlapping grids [4] or irregular cells [13], standard adaptive square cells are used in the fluid domain and at the boundaries to reduce the total number of unknowns without losing accuracy and to make the method simpler for implementation. Another known issue, namely the spurious pressure oscillations on moving structures induced by employing the immersed boundary method (IBM), is resolved in this study by solving a separate boundary value problem (BVP) for a Lagrangian acceleration potential. In contrast, solving a similar BVP for the corresponding Eulerian acceleration potential is far less satisfactory due to the involved second derivatives of the velocity potential in the body-boundary condition, which are very difficult to calculate accurately in an IBM-based approach. The accuracy and robustness of the proposed IB-AHPC method are demonstrated by solving a radiation problem of a harmonically heaving circular cylinder at the free surface in large motions and at high frequencies.

We also conducted an in-depth investigation on the low-pass filters applied on the free surface. To eliminate saw-tooth instabilities, typically, off-centered selective filters (SFs) are used close to the ends of the free surface and centered Savitzky–Golay (SG) filters are applied elsewhere. Our analyses show that care should be taken when applying off-centered SFs close to the waterline due to the presence of evanescent modes. An optimized 13-point, 10^{th}-order filter is also proposed and implemented in our study. Different from the classical SG(13,10) filter, this optimized filter is able to completely eliminate the saw-tooth waves with wave length of $2\Delta x$, where Δx represents the horizontal grid resolution on the free surface.

2 Lagrangian acceleration potential method for the IB-AHPC

The Harmonic Polynomial Cell (HPC) method was originally proposed by Shao and Faltinsen [8, 9] to solve the Laplace equation. In this work, to reduce the total number of cells without losing accuracy, adaptive quad-tree cells are employed close to the free-surface and structure boundaries. As shown in Fig. 1, the free surface and the body boundary are treated as immersed boundaries, and all colored nodes will be imposed with corresponding conditions. The basics of the HPC method will not be presented here, and interested readers are referred to [4, 8, 9]

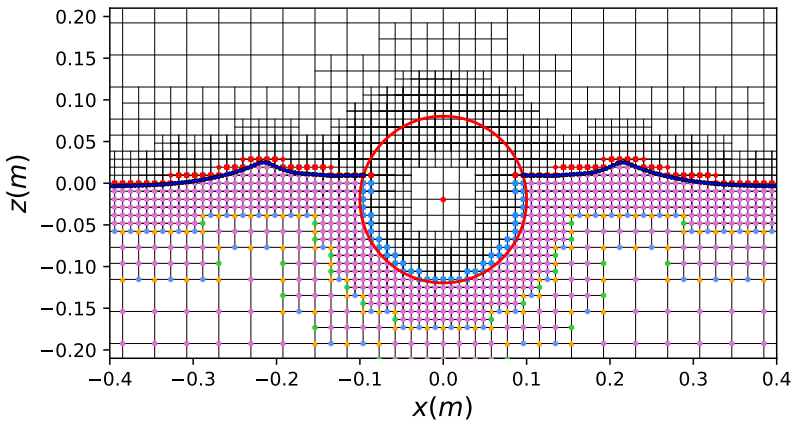

Figure 1: Snapshot of adaptive Cartesian grid system for a forced heaving circular cylinder at the free surface.

The hydrodynamic pressure on structures can be calculated by the Bernoulli's equation $p = -\rho(\varphi_t + \frac{1}{2}|\nabla\varphi|^2 + gz)$, where φ_t is the time derivative of the velocity potential, also called the acceleration potential. Since φ_t also satisfies the Laplace equation, it can be obtained by solving another separate BVP. In the Eulerian acceleration method (EAPM), the corresponding body-boundary condition is given as [14]

$$\frac{\partial\varphi_t}{\partial n} = (\dot{\mathbf{U}}_c + \dot{\omega}_c \times \mathbf{r}) \cdot \mathbf{n} + (\omega_c \times \mathbf{n}) \cdot (\mathbf{U}_c - \nabla\varphi) - (\mathbf{U}_c + \omega_c \times \mathbf{r}) \cdot (\mathbf{n} \cdot \nabla)\nabla\varphi, \tag{1}$$

*Corresponding author. E-mail addresses: ctong@mek.dtu.dk

where $\dot{\mathbf{U}}_c$ is the translating acceleration of the moving body and $\dot{\omega}_c$ is the angular acceleration about the rotation center. We denote this by EAPM since an Eulerian description is implied in this approach. As the IBM is used, the EAPM still introduces spurious oscillations. In contrast, the Lagrangian acceleration potential method (LAPM) [3], works excellently in eliminating spurious oscillations. A generalized material derivative of the velocity potential is defined as:

$$\Psi = \frac{D\varphi}{Dt} = \frac{\partial \varphi}{\partial t} + \mathbf{V} \cdot \nabla \varphi, \tag{2}$$

where $D\varphi/Dt$ denotes the time derivative of φ following a point that moves with the rigid-body velocity $\mathbf{V} = \mathbf{U}_c + \omega_c \times \mathbf{r}$. $\Psi(x, z, t)$ satisfies the Laplace equation, so that we can define a BVP for Ψ in the same way as the velocity potential. On the free surface, the Dirichlet boundary condition is given as:

$$\Psi = \mathbf{V} \cdot \nabla \varphi - \frac{1}{2} |\nabla \varphi|^2 - g\eta. \tag{3}$$

At a moving body surface, the body-boundary condition is given as:

$$\frac{\partial \Psi}{\partial n} = \dot{\mathbf{V}} \cdot \mathbf{n} + \mathbf{V} \cdot (\omega_c \times \mathbf{n}). \tag{4}$$

By comparison, this boundary condition for Ψ is simpler than that for the Eulerian acceleration potential in Eq. (1). In contrast to Eq. (1), Eq. (4) does not involve any derivatives of the velocity potential. This was seen to significantly improve the accuracy of the calculated hydrodynamic loads when using the IBM for a moving body. Direct comparison between the EAPM and LAPM will be presented and discussed during the workshop in detail.

3 Case study: Forced heaving of a circular cylinder in still water

The radiation problem of a semi-submerged circular cylinder harmonically heaving on the free surface is considered here to test the capability of this numerical model for simulating wave-body interaction. The center of cylinder is initially placed at the undisturbed free surface in the middle of the numerical water wave tank. The radius of the cylinder is $R = 0.1m$ and the non-dimensional heaving amplitude is $\sigma_{heave} = \eta_a/R = 0.2$. The heave motion is given as $\eta_{heave}(t) = -\eta_a \sin \omega t$. The length of the wave tank is ten times the wavelength $L_{tank} = 10\lambda$, and the considered water depth is larger than half of the wavelength and set to be $h = 15R$. Here the wavelength λ is found by the linear dispersion relation. A ramp function is applied to gradually start the motion within $t_{ramp} = 4T$, where T is the wave period.

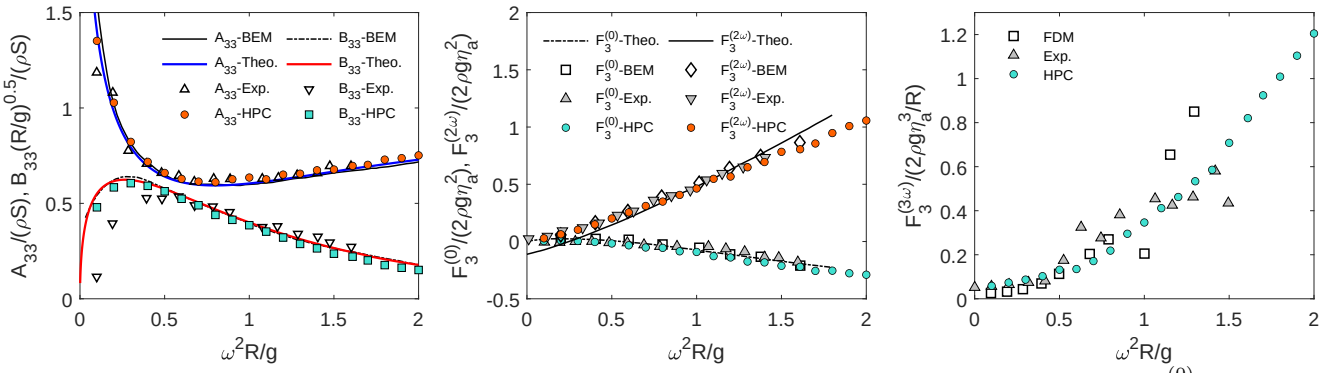

Figure 2: Heaving added mass and damping coefficients, normalized mean Fourier force-component $F_3^{(0)}$, second-order heave force $F_3^{(2\omega)}$ and third-order heave force $F_3^{(3\omega)}$ for the cylinder. Here ρ is the fluid density, and $S = 0.5\pi R^2$ is the mean submerged area of the cylinder section.

A Fourier analysis is performed on the time history of heaving force on the cylinder to determine the hydrodynamic added mass A_{33} and the damping B_{33}, the mean heave force $F_3^{(0)}$, the second-order heave force component $F_3^{(2\omega)}$ and the third-order heave force $F_3^{(3\omega)}$ for non-dimensional frequency $\omega^2 R/g$ ranging from 0.2 to 2.0. They are presented in Fig. 2 in normalized form. In the plot of A_{33} and B_{33}, the theoretical solutions of [12], the Boundary Element Method (BEM) results of [10], experimental results from [15] are compared with our IB-AHPC method. In the plot of $F_3^{(0)}$ and $F_3^{(2\omega)}$, the theoretical results of [6], fully-nonlinear BEM results of [11], experimental measurements of [12] and the present numerical solutions are compared. In the plot of $F_3^{(3\omega)}$, the present results are compared with the experiments of [15] and the fully-nonlinear results based on Finite Difference Method (FDM) results of [5]. In spite of small deviations, our present numerical solutions are globally in good agreement with the reference solutions. The most inspiring thing is that our numerical model is capable of computing cases with non-dimensional frequency up to $\omega^2 R/g = 2.0$.

4 Low-pass filters on the free surface

It is known that off-centered SG filters [7] tend to amplify some wave components rather than suppress them [2]. To overcome this problem, the Selective Filters (SFs) developed in [1] can be applied to treat boundary problems without amplification at any wavelength. In the radiation problem, we found the SFs have influence on both the propagating waves and the evanescent wave modes near the cylinder. To get some insights on the effect of SFs, in particular on the evanescent modes, we use the linear analytical solution of a piston-type wavemaker to study the amplification portraits of different SFs presented in [1]. Taking the sum of the first three evanescent modes for example, Fig. 3 demonstrates the amplification portraits of the SFs for the first three evanescent wave modes, where the selective filters are referred as SF(a,b). Here a and b are the number of points to the left and to the right respectively. and N denotes the number of points per wavelength of the corresponding propagating wave. A^* and A denote the total amplitude after and before filtering respectively. The filtered data $f^*(x_i)$ is expressed as a convolution of the original data $f(x_i)$ as $f^*(x_i) = f(x_i) - \alpha \sum_{j=-a}^{b} d_j f(x_i + j\Delta x)$, where d_j is the SF(a,b) coefficient at stencil point j. Here an intensity parameter α $(0 \le \alpha \le 1)$ has been introduced to control the strength of the selective filter.

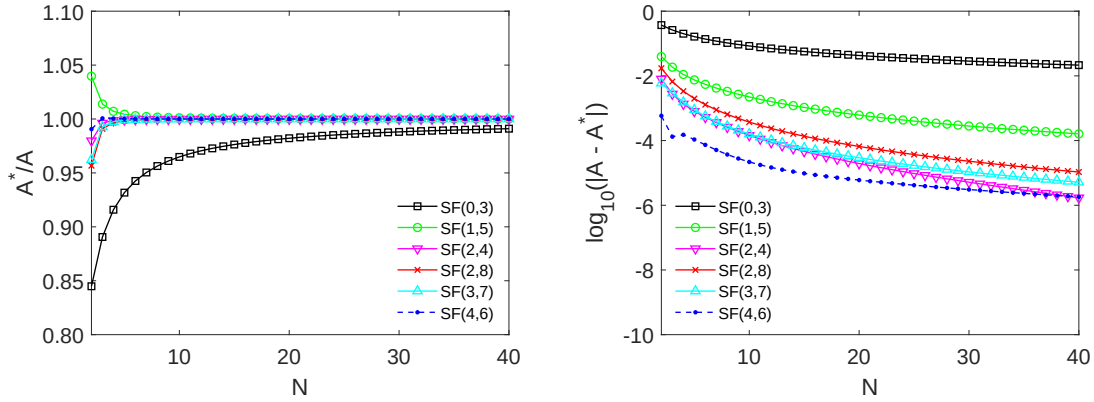

Figure 3: Amplification portraits of the selective filters from Berland et al. [1] for evanescent wave modes close to a piston wavemaker, $\alpha = 1$.

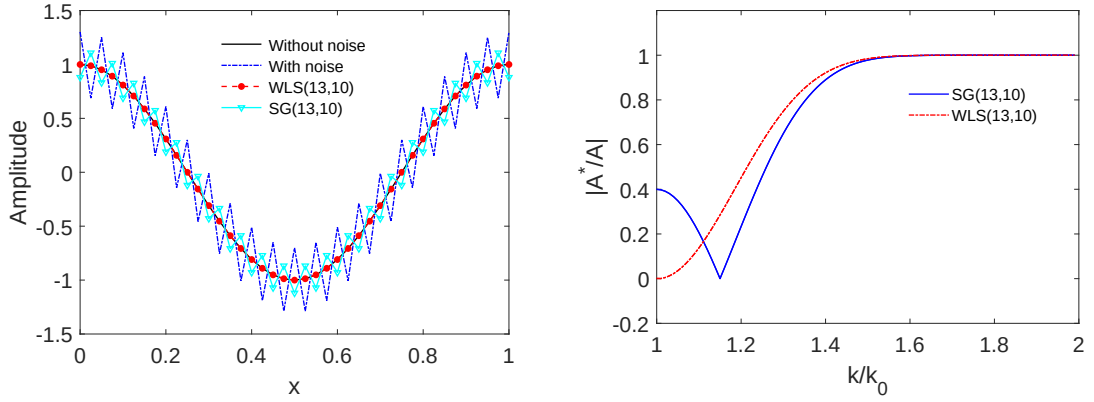

Figure 4: Comparison of original SG(13,10) filter and optimized WLS(13,10) filter.

The left plot in Fig. 3 indicates that the SF$(0,3)$ filter is the most dissipative for the evanescent modes comparing with other SF filters. The SF$(1,5)$ filter amplifies the amplitude, while all other filters exhibit a damping effect. In order to explicitly display differences of these filters, the amplification portrait is plotted in log scale in Fig. 3 (right). It can be seen that the amount of dissipation by the SF$(0,3)$ filter is 100 times larger than other filters. As the motion of the wavemaker increases in frequency and amplitude, stronger non-linearity of generated waves is expected. Given that the evanescent modes are more sensitive to the SF$(0,3)$ filter than the other filters, a smaller strength parameter α is needed for the SF$(0,3)$ filter to stabilize the computation without introducing too much dissipation to the higher-order wave harmonics.

Numerical instability occurs commonly with saw-tooth waves of around $2\Delta x$ wavelength. The original SG(13,10) filter is not able to completely damp those short wave components. In the present study, a new 13-point 10^{th}-order filter based on an optimized weighted least square (WLS) method has been applied. For brevity, we refer this filter as WLS(13,10). As shown in Fig. 4 (left), the WLS(13,10) filter is capable of eliminating undesired wave noise at wave number $k_0 = \pi/\Delta x$. The right of Fig. 4 also shows the dissipation of wave amplitude when $k = k_0$ for both the SG(13,10) and the WLS(13,10) filter. The coefficients in $f^*(x_i) = \sum_{j=-a}^{b} d_j f(x_i + j\Delta x)$ for the WLS(13,10) filter are given in Table. 1. Note however, that the WLS filter only works on the free surface away from the boundaries, as the same as the SG filter. That means, in our work, we still have to apply the SFs near the boundaries.

Table 1: Coefficients for the optimized WLS(13,10) filter.

$d_{-6}(d_6) = -2.44363800E-04$	$d_{-5}(d_5) = +2.93236558E-03$	$d_{-4}(d_4) = -1.61280107E-02$
$d_{-3}(d_3) = +5.37600357E-02$	$d_{-2}(d_2) = -1.20960080E-01$	$d_{-1}(d_1) = +1.93536129E-01$
$d_0 = +7.74207850E-01$		

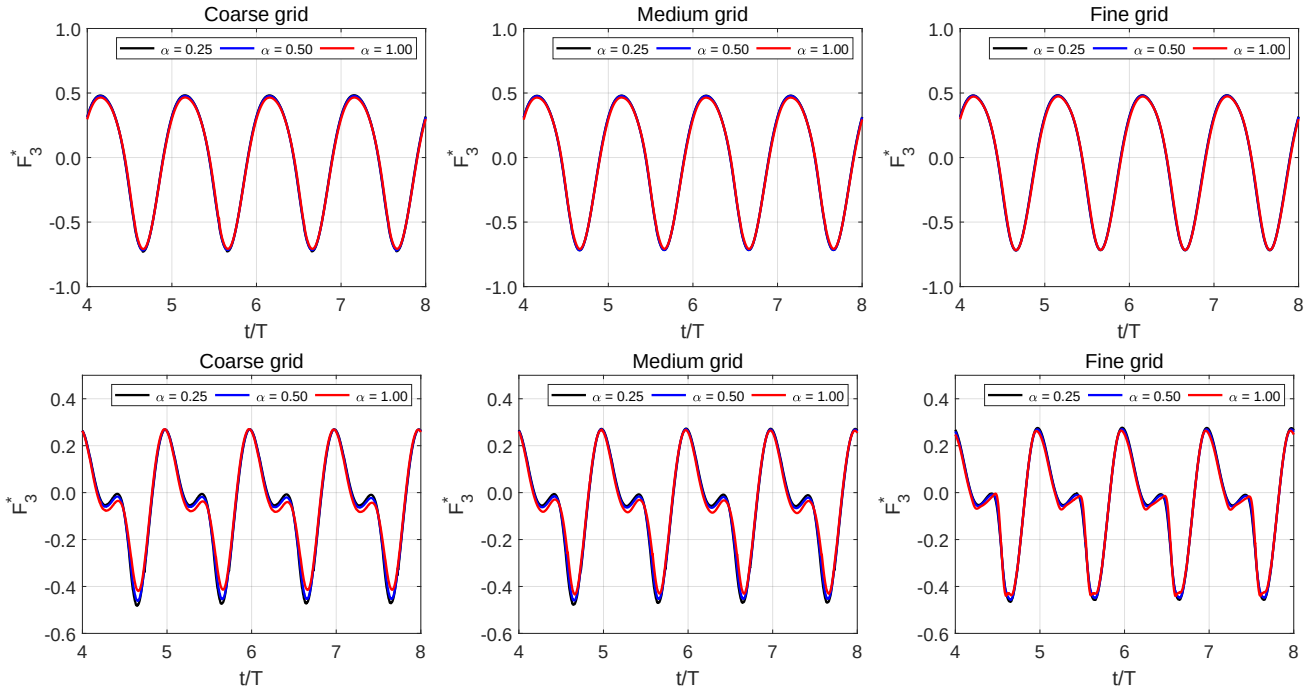

Figure 5: Non-dimensional heave force on cylinder for frequency $\omega^2 R/g = 1.0$ (first row) and for $\omega^2 R/g = 1.61$ (second row), with three grid refinements (coarse, medium and fine grid) and three strength parameters ($\alpha = (0.25, 0.50, 1.00)$).

Two cases with non-dimensional frequency $\omega^2 R/g = (1.0,\ 1.61)$ are chosen to investigate the influence of the strength parameter α of the selective filter on output results, shown in Fig. 5. Three grid refinements, i.e. $R/\Delta x = (10,\ 13,\ 20)$, and three values of the strength parameter, i.e. $\alpha = (0.25,\ 0.50,\ 1.00)$ are tested. Here, same value of α is applied to all selective filters on different locations of the free surface. It is obvious that the case with $\omega^2 R/g = 1.61$ is much more nonlinear than the one with $\omega^2 R/g = 1.0$. If we assume that the result with $\alpha = 0.25$ is the converged solution due to smaller dissipation induced, then we can expect that the force amplitude will reduce with increased filtering strength. The reduction is slight for case with $\omega^2 R/g = 1.0$, especially for the fine grid, which suggests the results are less sensitive to the α values in the case of weaker non-linearity. However, for the case with $\omega^2 R/g = 1.61$ on the fine grid, the time series of force deforms at the main and secondary troughs if $\alpha = 1.00$ is applied. This implies that, to accurately predict wave forces on structures when the non-linearity is strong, it is wise to use an appropriately small α. Several tests have been performed to suggest that $\alpha = 0.25$ is a reasonable choice for all frequencies displayed in Fig. 2. Note that we also tried smaller α, e.g. 0.1, but the computation requires much smaller time steps to produce stable solutions, which showed negligibly small differences with those using $\alpha = 0.25$.

Acknowledgment

This work is funded by the Chinese Scholarship Council (No.201906230317) and the Department of Mechanical Engineering at Technical University of Denmark.

References

[1] J. Berland, C. Bogey, O. Marsden, C. Bailly, J. Comp. Phys., 224, 637–62., 2007.
[2] G. Ducrozet, A. P. Engsig-Karup, H. B. Bingham, P. Ferrant, J. Comp. Phys., 257, 863–83, 2014.
[3] M. Greco, Ph.D. thesis. Norwegian University of Science and Technology, 2001.
[4] F. C. W. Hanssen, Ph.D. thesis. Norwegian University of Science and Technology, 2019.
[5] S. Kontos, Ph.D thesis, Technical University of Denmark, 2016.
[6] A. Papanikolaou, Proc. 13th Symp, 1980.
[7] A. Savitzky, M. J. Golay, Analytical chemistry, 1964.
[8] Y. L. Shao, O. M. Faltinsen, Americ. Soc. Mech. Eng. Digit. Collec., pp. 369–80, 2012.
[9] Y. L. Shao, O. M. Faltinsen, J. Comp. Phys., 274: 312–332, 2014.
[10] R. Skejic, Norwegian University of Science and Technology, 2008.
[11] H. Sun, Ph.D. thesis, Norwegian University of Science and Technology, 2007.
[12] F. Tasai, W. Koterayama, Rep. Res. Inst. Appl. Mech. Kyushu Univ , 24, 1–39, 1976.
[13] J. Wang, O. M. Faltinsen, W. Duan, Int. J. Numer. Meth. Eng. , 121, 3893–925, 2020.
[14] G. Wu, Z. Hu, Proceed.Roy. Soc. London , 460,2797–817, 2004.
[15] S. Yamashita, J. Soc. Nav. Arch. Japan , 61-9, 1977.